Published in final edited form as:
J Signal Process Syst. 2009 September 1; 2009: 1–6. doi:10.1007/s11265-010-0536-z.

Quality Map Thresholding for De-noising of Complex-Valued fMRI Data and Its Application to ICA of fMRI

Pedro A. Rodriguez,
Department of CSEE, University of Maryland, Baltimore County, Baltimore, MD 21250, USA

Nicolle M. Correa,
Department of CSEE, University of Maryland, Baltimore County, Baltimore, MD 21250, USA

Tom Eichele,
Department of Biological and Medical Psychology, University of Bergen, Bergen, Norway

Vince D. Calhoun, and
Department of ECE, The MIND Research Network and University of New Mexico, Albuquerque, NM 87131, USA

Tülay Adali
Department of CSEE, University of Maryland, Baltimore County, Baltimore, MD 21250, USA

Pedro A. Rodriguez: rodripe1@umbc.edu

Abstract

Although functional magnetic resonance imaging (fMRI) data are acquired as complex-valued images, traditionally most fMRI studies only use the magnitude of the data. FMRI analysis in the complex domain promises to provide more statistically significant information; however, the noisy nature of the phase poses a challenge for successful study of fMRI by complex-valued signal processing algorithms. In this paper, we introduce a physiologically motivated de-noising method that uses phase quality maps to successfully identify and eliminate noisy areas in the fMRI data so they can be used in individual and group studies. Additionally, we show how the developed de-noising method improves the results of complex-valued independent component analysis of fMRI data, a very successful tool for blind source separation of biomedical data.

Keywords

fMRI; ICA; Phase quality maps; De-noising

1 Introduction

FMRI is a well established tool for noninvasive investigation of brain function. It measures the hemodynamic response related to neural activity in the brain or spinal cord of humans or other animals [1].

FMRI is natively acquired as complex-valued spatiotemporal data; however, usually only the magnitude images are used for analysis. The phase images are usually discarded, since their noisy nature poses a challenge for successful study of fMRI when the processing is performed in the complex domain [2]. Recent studies have identified the presence of novel information in the phase, which can be utilized to better understand the brain function [3].

Correspondence to: Pedro A. Rodriguez, rodripe1@umbc.edu.

Moreover, data-driven techniques, such as independent component analysis (ICA), provide flexible models and have shown substantial promise for studying the magnitude and complex-valued fMRI data [4–6]. These studies have shown the importance of developing robust algorithms for de-noising complex-valued fMRI data.

Some complex-valued fMRI studies partially alleviate the noise issue by using smaller less noisy portions of the data, as done in [2]. In [4], the authors use a heuristically motivated thresholding and edge erosion technique, which fails to eliminate unreliable voxels—3D pixels—in high contrast areas of the complex images. In this paper, we develop a phase de-noising method that employs a physiologically justified approach to remove the noise.

Our quality map phase de-noising (QMPD) method allows the effective identification and elimination of noisy regions in the complex-valued fMRI data. Phase quality maps have been used in complex-valued signal applications such as radar to identify noisy areas in the phase [7]. Here, we demonstrate the usefulness of phase quality maps to detect noise due to aliasing and measurement errors, and develop an effective method to use these maps to eliminate corrupted regions in complex-valued fMRI data. To show the effectiveness and benefits of this method, we use it as a preprocessing step in complex-valued ICA of fMRI data. In this study, we choose a complex-valued ICA algorithm that uses nonlinear decorrelations with a sigmoid nonlinear function introduced in [5]. The results show significant improvement in performance over the heuristically motivated thresholding and edge erosion technique introduced in [4].

In Section 3, we describe the quality maps, how to calculate them, and how we use them to detect and eliminate unreliable volumes in the fMRI data using the QMPD method. The results from denoising fMRI data using QMPD are shown in Section 4. The benefits of the QMPD method on the performance of ICA of fMRI data are shown in Section 4.3. The ICA results are presented using an innovative visualization method based on Mahalanobis distance (Z_c), first introduced in [8], which incorporates both the magnitude and the phase in one measure in the estimation of voxels of interest. In [8], we also sucessfully applied some of the techniques described here in the pre-processing steps of a group ICA study that focus on alleviating the inherent phase ambiguity of complex-valued ICA.

2 Background

2.1 ICA of fMRI Data

Independent component analysis has emerged as an attractive analysis tool for discovering hidden factors in observed data and has been successfully applied for data analysis in a wide array of applications [9–11]. Especially in the case of fMRI analysis, it has proven particularly fruitful [12,13]. By using a simple generative model based on linear mixing, ICA yields two varieties of decompositions of the fMRI data: spatial ICA and temporal ICA. Spatial ICA has so far dominated the application of ICA to fMRI due to the nature of its key assumption that the data set consists of spatially independent components, which are linearly mixed and spatially fixed [14,15]. Localization and connectionism, two of the main characteristics of the brain [16] imply that different areas of the brain are responsible for different functions and there is either highly localized or functionally distributed activity in spatially independent areas.

We can form a matrix $\mathbf{X} \in \mathbb{C}^{T \times V}$ using the fMRI data such that the lth row is formed by flattening the volume image data of V voxels, at time instant l. In spatial ICA of fMRI data, we assume a simple linear mixing model such that $\mathbf{X} = \mathbf{AS}$, and determine *both* the activation maps and the corresponding waveforms, i.e., both $\mathbf{S}$ and $\mathbf{A}$, typically without

constraining either. The additional assumption we impose is that the rows of matrix **S** represent observations of statistically independent random variables.

Thus, spatial ICA finds systematically nonoverlapping, temporally coherent brain regions without constraining the temporal domain. A principal advantage of this approach is its applicability to cognitive paradigms for which detailed a priori models of brain activity are not available. Following its first application by McKeown et al. [13], ICA has been successfully used in a number of exciting fMRI applications, especially in those that have proven challenging with the standard regression-type approaches. These include identification of various signal types (e.g., task-related, transiently task-related, and physiology-related signals) in the spatial or temporal domain, analysis of multisubject fMRI data, incorporation of a priori information to improve the estimates, clinical applications, and for the analysis of complex-valued fMRI data. A comprehensive review of ICA approaches for fMRI data along with main references in the area is given in [17].

In spatial ICA, the number of components corresponds to the number of time-points, which in general are in the order of 100s, and for temporal ICA, they correspond to the number of voxels that are much higher. Hence, in both cases, a principal component analysis (PCA) stage traditionally precedes the ICA algorithm that is used to whiten the data and to determine the effective model order. Information theoretic criteria such as Akaike's Information Criterion, and the Minimum Description Length (MDL)—or the Bayesian Information Criterion—arise as natural solutions for determining the effective order of the components [18].

2.2 Complex ICA

For complex ICA, if we use the notation based on random variables, we start with the generative model, $\mathbf{x} = \mathbf{A}\mathbf{s}$, where $\mathbf{x}, \mathbf{s} \in \mathbb{C}^N$ and $\mathbf{A} \in \mathbb{C}^{N\times N}$, and achieve demixing by estimating a weight matrix $\mathbf{W}$ such that $\mathbf{u} = \mathbf{W}\mathbf{x} = \mathbf{P}\Lambda\mathbf{s}$. Here, $\mathbf{P}$, a permutation matrix, represents the permutation ambiguity and Λ, a diagonal matrix, represents the scaling ambiguity of ICA, which has a magnitude and phase term in the complex-valued implementation of ICA. The entries of the multivariate vector $\mathbf{x}$ represent the mixture random variables and are replaced by the given observations for the application in question, e.g., by the volume image at time l for fMRI data analysis.

To achieve independence of the sources s_k that form the source vector $\mathbf{s}$, an appropriate measure of independence has to be selected to compute the demixing matrix $\mathbf{W}$. Determining statistical independence requires computation of higher-order statistics in the data, e.g., higher order moments and/or cumulants. Various practical ways of generating higher order statistics exist, either explicitly as in the approaches based on cumulants (e.g., JADE [19]), or implicitly through the use of nonlinear functions (e.g., Infomax [9]).

ICA approaches that rely on nonlinear functions to implicitly generate the higher-order statistics to achieve independence offer practical and effective solutions to the ICA problem. They have been observed to be less sensitive to outliers (i.e., bounded and slowly growing) and seem to be more reliable when estimating task-related and transiently-related sources when compared to other approaches based explicitly on cumulants [20]. Two such popular approaches are based on maximum likelihood (ML)—which can be shown to be equivalent to information maximization and nonlinear decorrelations—and maximization of negentropy (MN), which can be shown to be equivalent to ML when the demixing matrix is constrained to be unitary [21]. For both ML and MN, the algorithms are optimal when the form of the nonlinear function used in the cost function matches the form of the probability density functions (pdf) of the sources $s_k = s_{k,re} + js_{k,im}$, which in the complex case are described by the joint density $p(s_{re},s_{im})$. However, as discussed in [5], a number of simple functions from

the trigonometric family provide robust and effective solutions for the ICA problem in the complex domain as in the real case, or simple adaptive mechanisms can be employed to estimate the independent components in a deflationary mode as discussed in [22]. The developments in both [23] and [22] do not make any assumptions such as the circularity—rotation invariance—of source distributions, an assumption common in complex ICA, making these approaches more suitable to applications such as fMRI data. Since very little is known about the nature of the fMRI data when used in its native complex form, it is desirable to avoid making additional assumptions such as the circularity of source distributions.

3 Quality Map Phase De-noising (QMPD)

3.1 Phase Residues

The phase obtained from complex images can be derived ambiguously as modulo 2π of the actual—principal—value, and it is usually displayed in the interval $(-\pi,\pi]$. Assuming that phase aliasing does not occur during the collection process is equivalent to constraining phase jumps between adjacent pixels to less than $\pm\pi$ radians per sample everywhere [24]. Ideally, any absolute jump greater than π is due to phase wrapping, though varying noise, measurement errors and aliasing could also introduce actual jumps greater than π.

The border lines between two adjacent pixels where the signal has undergone a relative rotation of more than π (in either direction) are cutlines [25], and it is at the borders of these cutlines that residues, inconsistencies or poles, as they are known in the literature, occur. The two poles at the corners of a cutline are of opposite sign, and are hence called dipoles. There are various ways to identify and locate these cutlines, as discussed in detail in [24]. Residues—dipoles—caused by aliasing, noise or other defects tend to have high phase gradients in their vicinity. In our application, we use quality maps to identify these unreliable high gradient regions that should be eliminated from further processing.

3.2 Quality Maps and Masks for Phase De-noising

Quality maps are arrays of values that define the quality or goodness of each pixel in a given phase image [24], and are extensively used in phase unwrapping methods. In our de-noising application, we are interested in using quality maps that assign bad quality values to noisy areas in the complex images, therefore they should identify volumes in the data where the pixel phase values and their gradients exhibit high variation.

We use the phase derivative variance (PDV) map [24] in the QMPD method, based on the quality of results obtained in our study when comparing this map to others, and the fact that the PDV map is considered to be extremely robust in identifying noisy areas in phase images [24]. The PDV map is calculated as a root-mean square measure of the variances of the partial derivatives in the x- and y-directions of the phase image, such that high values represent low quality. In the PDV map, the $(m,n)th$ pixel value is computed as

$$z_{m,n}=\sqrt{\frac{\sum_{i,j=-(k-1)/2}^{(k-1)/2}\left(\Delta_{i,j}^{x}-\tilde{\Delta}_{m,n}^{x}\right)^{2}}{k^{2}}}+\sqrt{\frac{\sum_{i,j=-(k-1)/2}^{(k-1)/2}\left(\Delta_{i,j}^{y}-\tilde{\Delta}_{m,n}^{y}\right)^{2}}{k^{2}}} \quad (1)$$

where for each sum the indexes (i, j) range over the $k \times k$ window centered at the pixel (m,n). The terms $\Delta_{i,j}^{x}$ and $\Delta_{i,j}^{y}$ are the partial derivatives—wrapped phase differences—of the

phase. The terms $\tilde{\Delta}^{x}_{m,n}$ and $\tilde{\Delta}^{y}_{m,n}$ are the averages of these partial derivatives in the $k \times k$ windows.

We, additionally, studied the following quality maps as candidates for QMPD: the phase variance map [24], the maximum phase gradient map [7], the pseudocorrelation quality map [24], and the second difference quality map [26]. Empirical results showed that the obtained maps were mostly similar to the PDV map; however, they were not as robust as the PDV map in clearly identifying noisy and unreliable pixels in regions of high contrast to noise ratio (CNR) in the complex images.

Quality maps are used to develop binary quality *masks*, which assign a "0" to unreliable pixels that should not be further analyzed. These quality masks are obtained by thresholding the quality maps. Simple thresholding values can easily be acquired by visually inspecting the quality values that are assigned to the majority of the gray matter areas of the brain. These areas exhibit low phase variation when compare to their surroundings, e.g., skull and background of the fMRI slices [3]. Pixels with very small values—0.2 radians in our implementation—in the PDV map correspond to areas of low phase gradients and hence, can usually be considered as having good quality. Additionally, we can implement the automatic threshold selection method described in [24, p. 85], and obtain similar threshold values.

3.3 QMPD Implementation

The steps of the QMPD method are summarized in Algorithm 1. The first step is to calculate the PDV quality map for each fMRI 2D slice image at every time point for the data collected from a specific subject. In the second step, we threshold all the obtained PDV quality maps to obtain a binary PDV mask for every time point, as described in Section 3.2. A value of "1" should indicate that a voxel has good quality.

It is desired at this point to obtain a single binary quality mask for every fMRI 2D slice that can be applied to all the time points. The third step is to do a logical AND operation, across the time dimension, to all the obtained PDV masks. This step allows only voxels with good quality across the time dimension to survive the threshold.

In the fourth step, we perform a morphological closing operation, which consists of a morphological erosion step followed by a dilation step using a disk-shaped morphological structuring element with a two voxel diameter. This step eliminates any non-contiguous voxels in the background of the slices that may have survived the previous step. At this point, the resulting single quality masks, for every 2D fMRI slice, clearly highlight areas of high quality.

After obtaining the final quality masks, we multiply them with the original real and imaginary 2D fMRI slices. The final step consists of smoothing the resulting complex image. This smoothing step is common in fMRI analysis, since it helps to improve the CNR, but it is important to apply it after de-noising the fMRI data, since the smoothing filter can adversely spread the detrimental effects of the noisy areas to adjacent voxels. A typical smoothing filter utilizes a $10 \times 10 \times 10$ mm^3 full width at half-maximum Gaussian kernel.

4 Results

In Section 4.1, we introduce the fMRI data used in the results presented in this paper. In Section 4.2, we present the results of the QMPD method when applied to the complex-valued fMRI data. Finally, in Section 4.3 we show how the introduced de-noising and phase correction methods improve the performance of complex-valued ICA of fMRI.

4.1 fMRI Data

The dataset used in this paper is from sixteen subjects performing a finger-tapping motor task while receiving auditory instructions. The paradigm involves a block design with alternating periods of 30 s *ON* (finger tapping) and 30 s *OFF* (rest). The experiments were performed on a 3T Siemens TRIO TIM system with a 12-channel radio frequency (RF) coil. The fMRI experiment used a standard Siemens gradient-echo EPI sequence modified to store real and imaginary data separately. The data was pre-processed for motion correction and spatial normalization into standard Montreal Neurological Institute space using the MATLAB Toolbox for Statistical Parametric Mapping (SPM).1

As an example, the phase and magnitude from subject one at the first time point (out of 165 time points) is displayed in Figs. 1 and 2. Starting from the top left slice and then moving right and down, we can see the slices as if were going from the top of the head towards the neck. Phase images were zero padded to add separation between slices for display purposes.

4.2 De-noising Results

4.2.1 QMPD Quality Maps and Masks—Figure 3 shows the PDV maps calculated for the phase image slices of subject one shown in Fig. 1. The PDV maps were calculated by using Eq. 1 with $k = 3$, which defines the smallest possible square window that can be used to calculate variances. The maps are converted to Z-scores and thresholded at $|Z| > 1$ to only show areas of bad quality displayed over the background anatomical image. Z-score is a dimensionless quantity that measures how many standard deviations an observation is above or below the mean of the entire dataset. It can be seen that the PDV maps assign low quality values to the background of the slices and even to some areas inside the high CNR regions. These low quality areas inside the brain gray matter will be shown to contain phase residues and noisy artifacts in Section 4.2.2.

Figure 4 shows the quality masks obtained after applying the QMPD thresholding step to the PDV maps used to create Fig. 3. We can see that there are some background voxels near the corners of the slices that were erroneously assigned as good quality voxels. These erroneous good quality voxels are eliminated after applying the QMPD logical AND and morphological closing operation steps. In Fig. 5, we can see the resulting quality binary masks obtained for each fMRI slice after applying the QMPD method to the fMRI data of subject one. These masks are then used to de-noise the complex-valued fMRI slices across all the time points.

4.2.2 QMPD De-noising Examples—In Figs. 6, 7, and 8, we show an example of the results of multiplying the obtained PDV quality mask by the magnitude, phase, and residue images, respectively, of fMRI slice number seven shown in Fig. 1. The area inside the brain gray matter eliminated by the mask in this slice belongs to the orbitofrontal cortex, which is well known to suffer from susceptibility artifacts from the air in the sinuses. Although this area was inside a high CNR region, the quality mask clearly indicated that it was noisy and unreliable. Figure 8, confirms that all the phase residues are eliminated by the QMPD method.

In Fig. 9 we present a QMPD mask obtained from the data of all the subjects in our experiment using the approach for groups of subjects as discussed in [8]. This approach is used to combine the QMPD mask of multiple subjects into a single one that can then be used to identify good quality voxels across all subjects. It can clearly be seen that the eliminated regions in the fMRI slices correspond to known physiologically noisy areas like the large

[1]SPM, URL: http://www.fil.ion.ucl.ac.uk/spm/software/spm5

susceptibility artifacts around the nasal and frontal sinuses, the ear canal, the large vessels on the base of the brain, the Willis circle (large arteries) and the draining veins such as the transverse sinus.

4.3 QMPD Complex-Valued ICA of fMRI Results

We demonstrate the importance of denoising using QMPD when it is used in a preprocessing step in analysis of the complex-valued fMRI data. When performing spatial ICA of fMRI data [17], we use PCA to reduce the dimensionality of the complex-valued fMRI data. The number of effective components is selected as 30 using the MDL criterion for complex valued data as in [4]. We then apply complex-valued ICA using nonlinear decorrelations with a sigmoid nonlinear function [5]. Estimated sources in ICA are usually presented using Z-score thresholded magnitude images to highlight the voxels of interest, therefore ignoring the phase information. The visualization method we use here takes into account the phase by using a two dimensional Mahalanobis distance metric in the real and imaginary data of the estimated sources given by

$$Z_{c_{k,i}} = \sqrt{[\widehat{\mathbf{s}}_{k,i} - \mu_k]^{\mathrm{T}} \mathbf{C}_k^{-1} [\widehat{\mathbf{s}}_{k,i} - \mu_k]} \tag{2}$$

where $\hat{\mathbf{s}}_{k,i} = [\hat{s}_{k,i,re}, \hat{s}_{k,i,im}]^{\mathrm{T}}$; and $\boldsymbol{\mu}_k$ and $\mathbf{C}_k$ are the corresponding mean and covariance of the estimated sources. If the covariance matrix is the identity matrix, the Mahalanobis distance reduces to the Euclidean distance. The Mahalanobis distance is equal to the absolute value of the Z-score metric when the data is univariate. Therefore, the obtained Z_c maps are usually thresholded using the same typical values used in practice to threshold Z-score maps when working with magnitude only fMRI data, e.g., 2, 3 and 4.

The obtained spatial independent components were compared to the components obtained by the ICA algorithm after using a heuristic magnitude thresholding and edge erosion (MTEE) method, previously used in [4]. This method uses a magnitude mask that is created by assigning a “1” to a voxel with a magnitude higher than the average magnitude of all the slices. This mask only eliminates low CNR regions in the fMRI data and ignores areas affected by susceptibility and under sampling issues that occur inside high CNR regions.

The normalized correlation value between the QMPD binary masks and the MTEE masks for the fMRI slices of this subject was 0.93. The QMPD masks covered 0.23% less area than the MTEE masks. These differences are due to the fact that high CNR regions, with phase residues, are not filtered out by the MTEE masks. Similar correlation results were obtained for the rest of the subjects.

To evaluate the performance of the QMPD and the MTEE method, we focus on the differences in the estimation of two functionally interesting components: a temporal lobe and a motor-task related component. Figure 10a shows the Mahalanobis distance (Z_c), phase and magnitude spatial maps of one of the obtained spatial components, associated with the performed task. The Z_c map was thresholded at $Z_c > 2$ to identify voxels of interest. This component corresponds to the spatial activation map of the temporal lobe, which is coupled to the auditory instructions of the finger-tapping motor task. Figure 10b shows the temporal lobe Z_c, phase and magnitude spatial activation maps obtained by the ICA of the MTEE pre-processed fMRI data. The segmentation of the temporal lobe is not as clear and is noisier than the results obtained with the QMPD method. Table 1 shows the number of active voxels, and the maximum and mean of the Mahalanobis distance values in the temporal lobe for both algorithms. Although the MTEE method has a slightly higher maximum

Mahalanobis distance value, it can be clearly seen that the QMPD method sucessfully identified more voxels of interest with higher overall values.

In Fig. 11, we show a motor task-related component obtained from another subject using the QMPD and the MTEE methods, respectively, for pre-processing in a complex-valued ICA application with the circular nonlinear function proposed in [27]. This spatial component was chosen because it had the highest regression coefficient when regressed with the calculated ideal temporal hemodynamic response. Average results from this sujbect and other nine are presented in Table 2. The ICA results obtained with the QMPD method once again provides higher overall Z_c values and a larger number of active voxels (17% more) as compared to those obtained with the MTEE method.

The difference in performance using QMPD preprocessing is not as significant for the task-related, motor component, when compared to the temporal lobe component. However, it is important to note that using ICA, the task-related component was estimated consistently in most of the cases, whereas this was not the case for the temporal lobe component. Additionally, the thresholding metric that we have introduced for the spatial maps, the Mahalanobis Z-score is also important in successfully extracting the task-related active voxels from the noisy and bad quality voxels that may survive in the background using the heuristic MTEE preprocessing method.

In most of our experiments the MTEE failed to estimate other relevant components, such as the temporal lobe, in some of the subjects. Additionally, in some experiments the obtained components look noisier and physiologically meaningless when compared to the QMPD method results.

5 Discussion

We implemented a simple, yet effective, method to robustly denoise fMRI complex-valued data. The QMPD method accurately identifies and eliminates areas of the fMRI images that are corrupted by noise, measurement errors, and aliasing. QMPD can be used as a pre-processing step by any fMRI complex analysis algorithm. QMPD should always be applied prior to the typical smoothing step, which improves the CNR of fMRI data, to avoid spreading the detrimental effects of the noisy regions to adjacent voxels. In this paper, we showed how QMPD provides significant improvement in the sensitivity of complex-valued ICA results compared to a previously implemented pre-processing method. Even though using QMPD, we might be working with smaller number of voxels, we obtain higher activation levels and larger areas of meaningful activation. Other studies using complex-valued fMRI data either segmented specific areas of the brain or only used the magnitude image, thus not only partially de-noising the data, but also possibly losing clean data. QPMD thus provides the ability to work with all the good quality voxels, and hence improves the statistical power of the complex analysis algorithms.

Acknowledgments

This work is supported by the NSF grants NSF-CCF 0635129 and NSF-IIS 0612076.

References

1. Huettel, SA.; Song, AW.; McCarthy, G. Functional magnetic resonance imaging. Sinauer Associates; 2004.
2. Calhoun VD, Adali T, Pearlson GD, van Zijl PCM, Pekar JJ. Independent component analysis of fMRI data in the complex domain. Magnetic Resonance in Medicine. 2002; 48:180–192. [PubMed: 12111945]

3. Feng Z, Caprihan A, Blagoev KB, Calhoun VD. Biophysical modeling of phase changes in Bold FMRI. NeuroImage. 2009 (in press).
4. Xiong, W.; Li, YO.; Li, H.; Adali, T. On ICA of complex-valued fMRI: Advantages and order selection. Proc. IEEE int. conf. acoust., speech, signal processing (ICASSP); Las Vegas, Nevada. 2008.
5. Adali, T.; Kim, T.; Calhoun, VD. Independent component analysis by complex nonlinearities. Proc. IEEE int. conf. acoust., speech, signal processing (ICASSP); Montreal, Canada. 2004. p. 525-528.
6. Calhoun, VD.; Adali, T.; Li, YO. Independent component analysis of complex-valued functional MRI data by complex nonlinearities. Proc. IEEE int. symp. bio. imag. (ISBI); Arlington, VA. 2004.
7. Cho BL, Kong YK, Kim YS. Quality map extraction for radar interferometry using weighted window. Electronic Letters. 2004; 40(8)
8. Rodriguez, P.; Adali, T.; Li, H.; Correa, N.; Calhoun, V. Phase correction and denoising for ICA of complex fMRI data. Proc. IEEE int. conf. acoust., speech, signal processing (ICASSP); 2010.
9. Bell A, Sejnowski T. An information maximization approach to blind separation and blind deconvolution. Neural Computation. 1995; 7:1129–1159. [PubMed: 7584893]
10. Hyvarinen, A.; Karhunen, J.; Oja, E. Independent component analysis. New York: Wiley; 2001.
11. Comon P. Independent component analysis: A new concept? Signal Processing. 1994; 36:11–20.
12. McKeown MJ, et al. Spatially independent activity patterns in functional magnetic resonance imaging data during the stroop color-naming task. Proceedings of the National Academy of Sciences of the United States of America. 1998; 95:803–810. [PubMed: 9448244]
13. McKeown MJ, et al. Analysis of fMRI data by blind separation into independent spatial components. Human Brain Mapping. 1998; 6(3):160–188. [PubMed: 9673671]
14. McKeown MJ, Sejnowski TJ. Independent component analysis of fMRI data: Examining the assumptions. Human Brain Mapping. 1998; 6:368–372. [PubMed: 9788074]
15. Biswal BB, Ulmer JL. Blind source separation of multiple signal sources of fmri data sets using independent component analysis. Journal of Computer Assisted Tomography. 1999; 23:265–271. [PubMed: 10096335]
16. Phillips CG, et al. Localization of function in the cerebral cortex. past, present and future. Brain. 1984; 107:327–361. [PubMed: 6421455]
17. Calhoun VD, Adali T. Unmixing fMRI with independent component analysis. IEEE Engineering in Medicine and Biology Magazine. 2006; 25(2):79–90. [PubMed: 16568940]
18. Adali T, Calhoun VD. Complex ICA of brain imaging data. IEEE Signal Processing Magazine. 2007; 24(5):136–139.
19. Cardoso JF, Souloumiac A. Blind beam forming for non-Gaussian signals. IEEE Proceedings Radar and Signal Processing. 1993; 140:362–370.
20. Correa N, et al. Comparison of blind source separation algorithms for fMRI using a new matlab toolbox: GIFT. ICASSP. 2005; 5:401–404.
21. Adali T, Li H, Novey M, Cardoso J. Complex ica using nonlinear functions. IEEE Transactions on Signal Processing. 2008; 56(9):4536–4544.
22. Novey M, Adali T. Complex ICA by negentropy maximization. IEEE Transactions on Neural Networks (TNN). 2008; 19(4):596–609.
23. Adali, T.; Li, H. A practical formulation for computation of complex gradients and its application to maximum likelihood. Proc. IEEE int. conf. acoust., speech, signal processing (ICASSP); 2007.
24. Ghiglia, DC.; Pritt, MD. Two-dimensional phase unwrapping. New York: Wiley; 1998.
25. Chavez S, Xiang Q, An L. Understanding phase maps in MRI: A new cutline phase unwrapping method. IEEE Transactions on Medical Imaging. 2002; 21(8):966–977. [PubMed: 12472269]
26. Herrat'ez MA, Gdeisat MA, Burton DR, Lalor MJ. Robust, fast, and effective two dimensional automatic phase unwrapping algorithm based on image decomposition. Applied Optics. 2002; 41:7445–7455. [PubMed: 12502302]
27. Anemuller J, Sejnowski TJ, Makeig S. Complex independent component analysis of frequency-domain electroencephalographic data. Neural Networks. 2003; 16(9):1311–1323. [PubMed: 14622887]

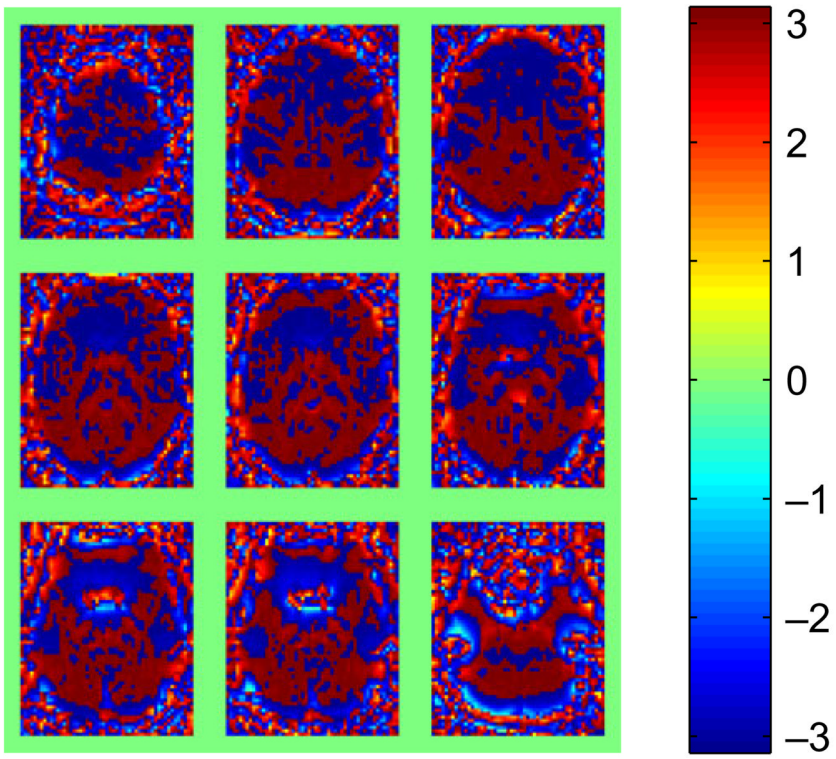

Figure 1.
Phase image (in radians) of 9 out of 46 slices corresponding to the first time point of subject one.

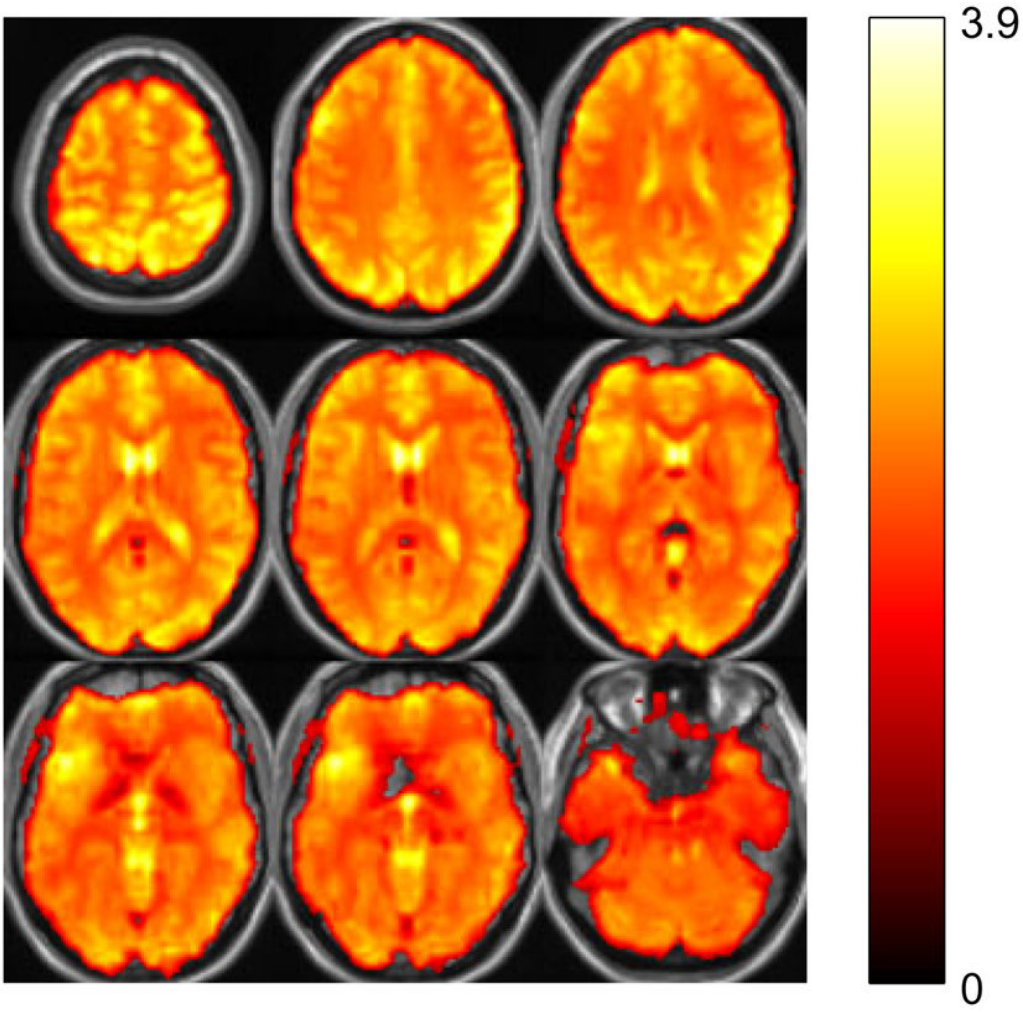

Figure 2.
Magnitude slices of subject one overlayed over an anatomical background image. Magnitude data was change to Z-scores and thresholded at $|Z| > 1$.

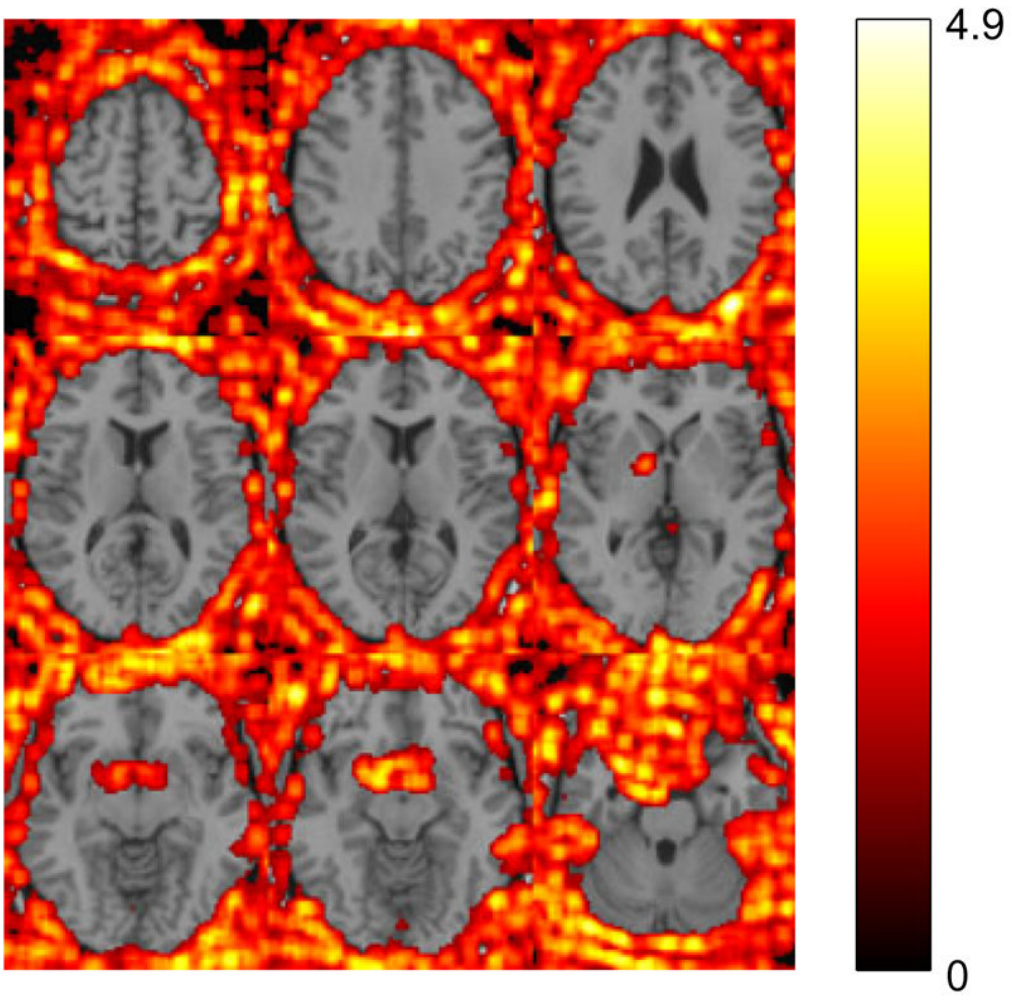

Figure 3.
PDV maps of phase images in Fig. 1. The maps were converted to Z-scores and thresholded at $|Z| > 1$ for display purposes.

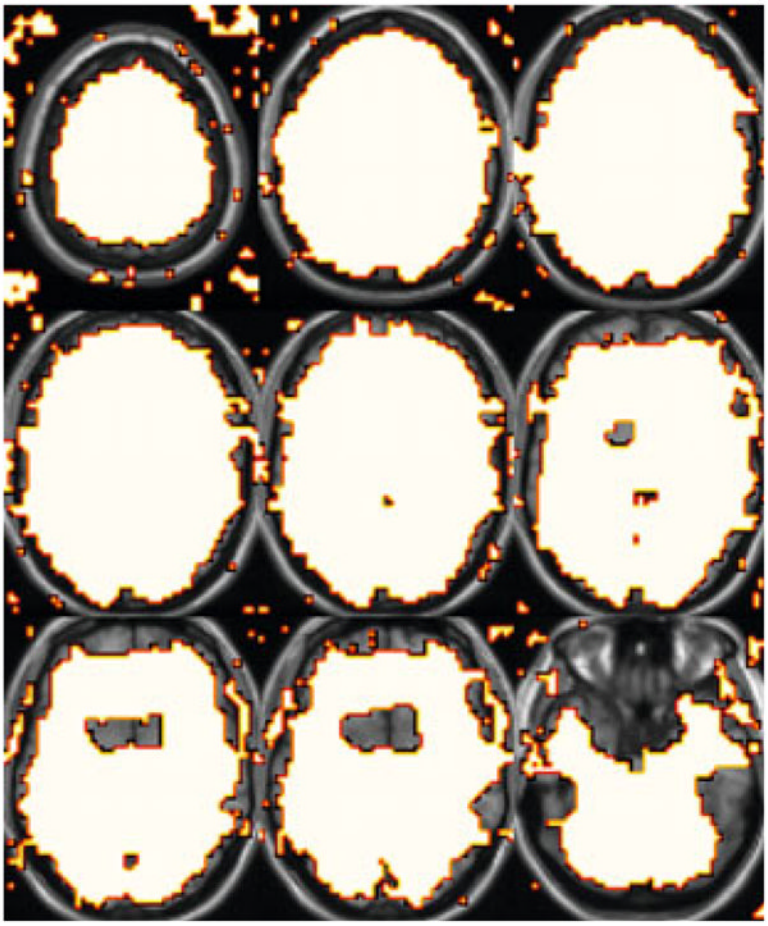

Figure 4.
Binary (white = 1) PDV quality masks obtained from thresholding the PDV maps used to create Fig. 3.

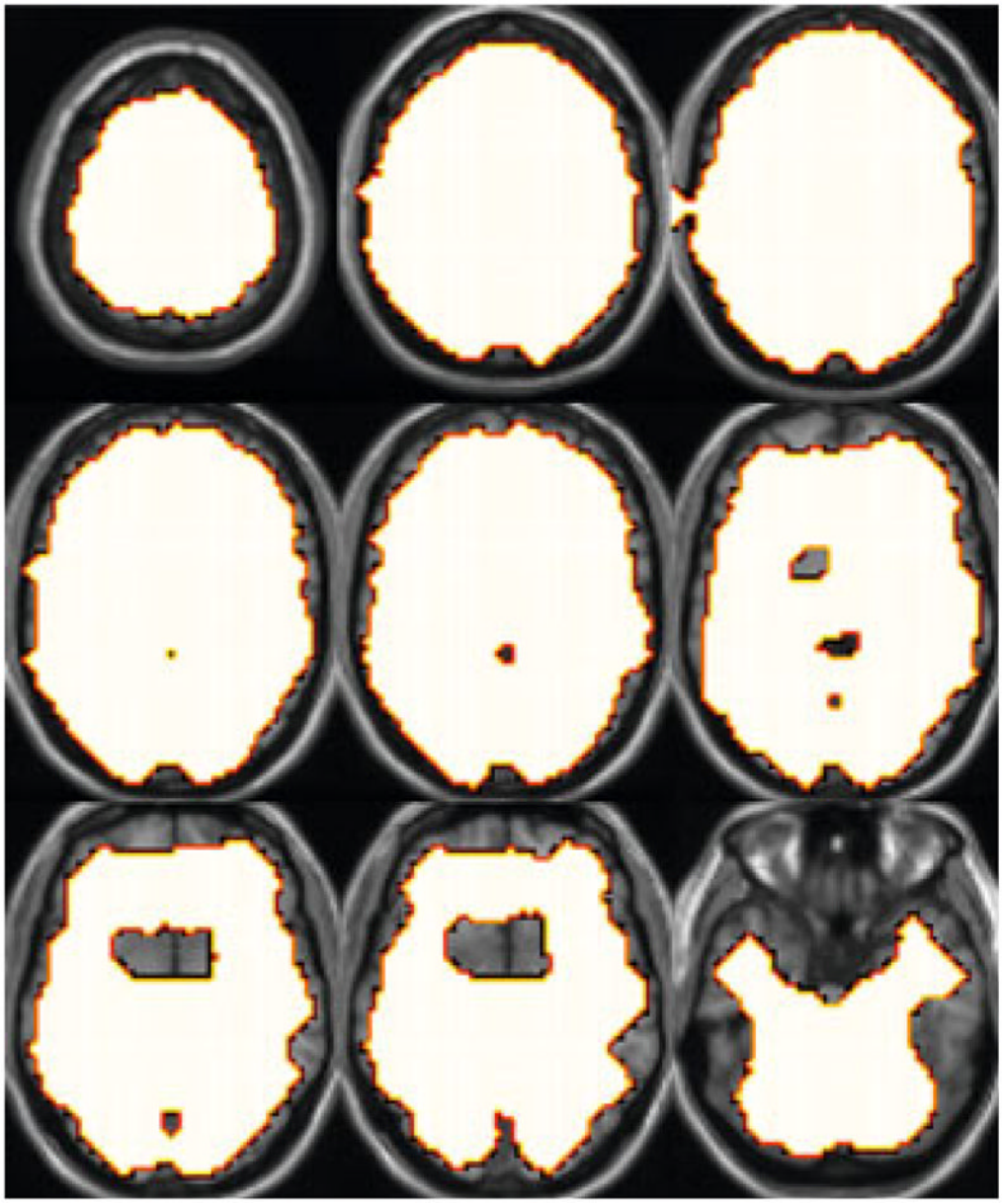

Figure 5.
Binary (white = 1) quality masks obtained after applying the QMPD method to the fMRI data of subject one.

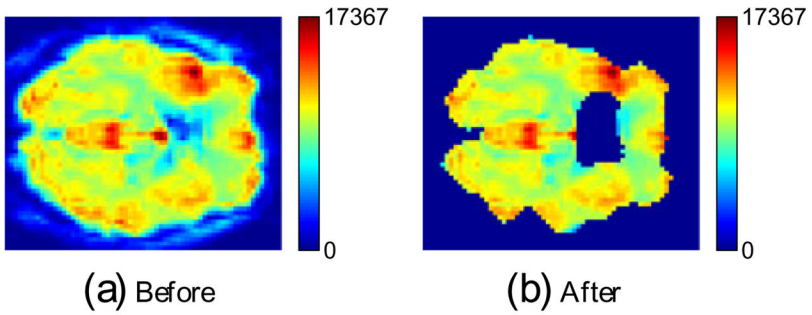

Figure 6.
Magnitude image of slice seven of subject one, at time point one, before and after multiplication by the quality mask.

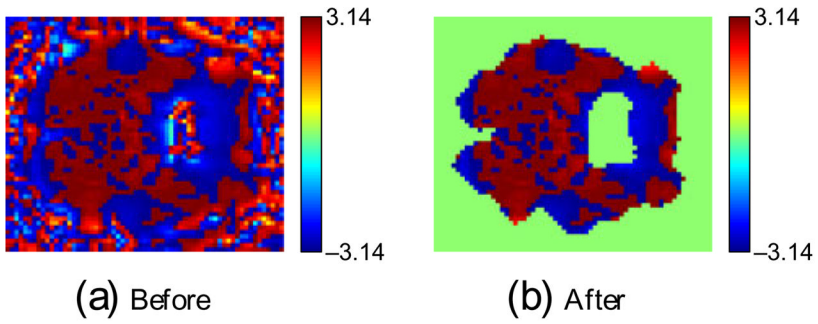

Figure 7.
Phase image (in radians) of slice seven of subject one, at time point one, before and after multiplication by the quality mask.

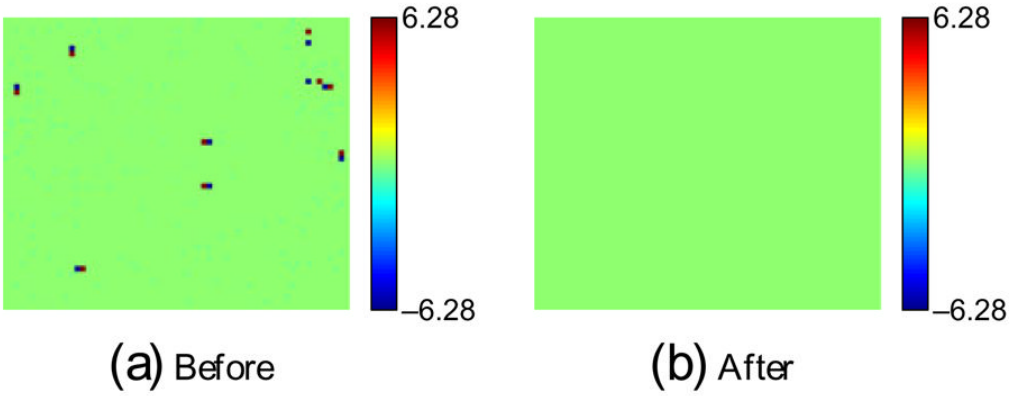

Figure 8.
Phase residues image (in radians) of slice seven of subject one, at time point one, before and after multiplication by the quality mask.

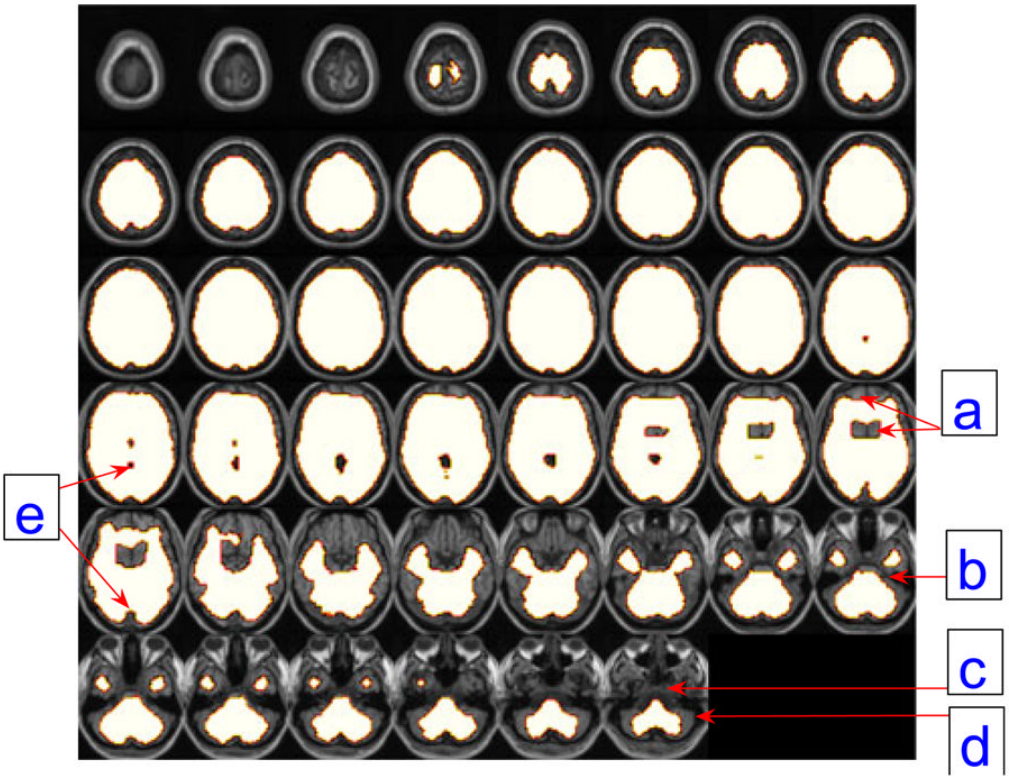

Figure 9.
QMPD mask obtained for all 46 slices obtained from multiple subjects. Eliminated regions correspond to known physiologically noisy areas like the large susceptibility artefacts around the nasal and frontal sinuses (*a*), the ear canal (*b*), the large vessels on the base of the brain (*e*), the Willis circle (*c*) and the draining veins, such as the transverse sinus (*d*).

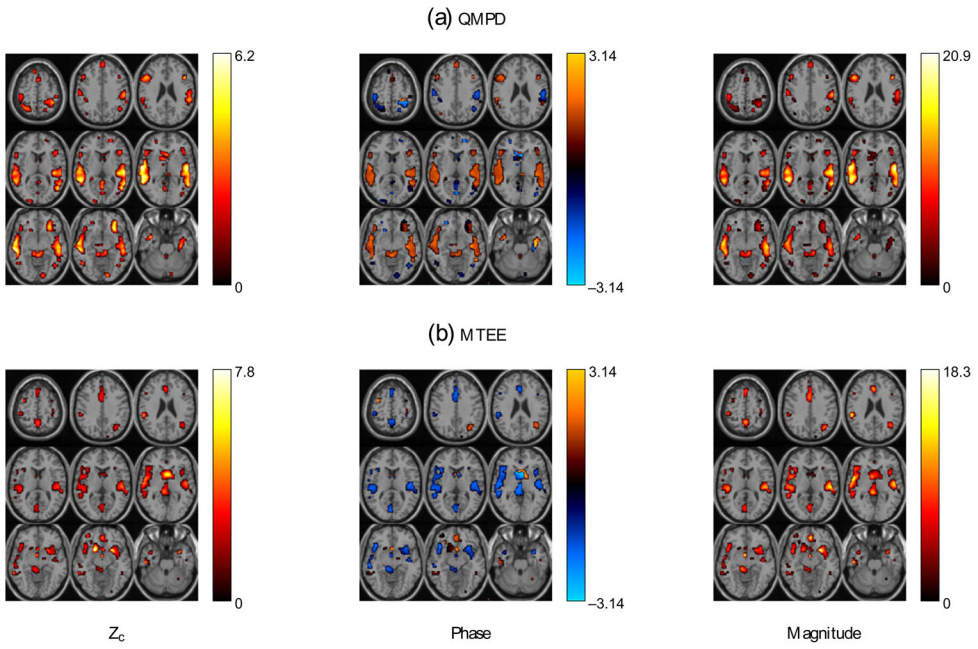

Figure 10.
Temporal lobe Z_C, phase and magnitude spatial activation map obtained from ICA algorithm using the **a** QMPD and the **b** MTEE method in the pre-processing steps. Voxels with a Z_C greater than 2 and good quality were identified as voxels of interest.

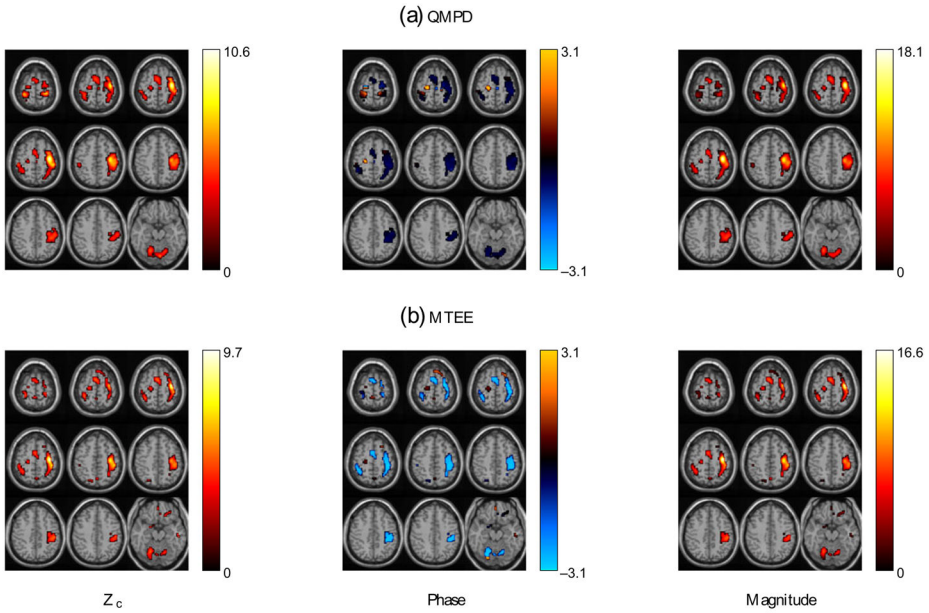

Figure 11.

Z_c, phase and magnitude of motor task related component obtained from ICA algorithm using the **a** QMPD and the **b** MTEE method in the pre-processing steps. Voxels with a Z_c greater than 3 and good quality were identified as voxels of interest.

Table 1

Results of complex-valued ICA using QMPD and MTEE for pre-processing.

Pre-processing method	Active voxels	Maximum Z_c score	Mean Z_c score
MTEE	492	10.40	2.90
QMPD	956	6.93	3.53

The number of active voxels is calculated by counting the number of voxels with a $Z_C > 2$ in the temporal lobe area.

Table 2

Results of complex-valued ICA using QMPD and MTEE for pre-processing in ten subjects.

Pre-processing method	Active voxels	Maximum Z_c score	Mean Z_c score
MTEE	619	13.27	4.77
QMPD	712	11.68	5.09

The number of active voxels is calculated by counting the number of voxels with a $Z_C > 3$ in the motor task identified voxels.

Algorithm 1

QMPD

1 Calculate PDV quality map ($\mathbf{P}_{vu}$) of each 2D fMRI slice v at every time point u using Eq. 1;

2 Threshold all $\mathbf{P}_{vu}$ by r (see Section 3.2) to obtain binary mask: $\mathbf{B}_{vu}$;

3 Keep all voxels with good quality across time dimension: $\mathbf{Q}_v = \prod_{u=1}^{U} \mathbf{B}_{vu}$;

4 Perform morphological closing operation to eliminate non-contiguous voxels in non-brain areas in $\mathbf{Q}_v$;

5 Multiply complex-valued (real and imaginary) fMRI slices v by corresponding $\mathbf{Q}_v$ mask;

6 Apply smoothing filter to surviving voxels.